

Improving the Dimensional Accuracy of Micro Parts 3D Printed with Projection-Based Continuous Vat Photopolymerization using a Model-Based Grayscale Optimization Method

Ege Guven^a, Yigit Karpat^{a,b,c}, Melih Cakmakci^{a,*}

^a*Department of Mechanical Engineering
Bilkent University, Ankara, 06800, Turkey*

^b*Department of Industrial Engineering
Bilkent University, Ankara, 06800, Turkey*

^c*UNAM – Institute of Materials Science and Nanotechnology
Bilkent University, Ankara, 06800, Turkey*

Abstract

Micro-scale additive manufacturing has seen significant growth over the past years, where improving the accuracy of complex micro-scale geometries is seen as an important challenge. Using grayscale images rather than black and white images during production is an effective method to improve the fabrication quality. This paper presents a model-based optimization method for improving the dimensional accuracy of parts using voxel-based grayscale dynamic optimization during continuous 3D printing. A detailed solidification model has been developed and used to estimate the curing dynamics of the resin used in 3D printing. The irradiance of the light beam projected for each pixel influences a larger volume on the resin than the targeted voxel. The proposed model-based method optimizes the images considering the light distribution from all closely related pixels to maintain the accuracy of the micro part. The results of this method have been applied to the printing of a complex 3D part to show that optimized grayscale images improve the areas with overcuring significantly. It is shown that the number of overcured voxels was reduced by 24.7% compared to the original images. Actual printing results from our experimental setup confirm the improvements in the accuracy and precision of the printing method.

Keywords: process planning, vat photopolymerization, modeling, dynamic optimization

1. Introduction

Vat Photopolymerization (VPP) is a popular method for obtaining polymer-based parts due to its fast production speed, flexibility of the objects that can be produced, and high accuracy [1], [2]. VPP can be used on its own or along with various other additive manufacturing processes to produce complex parts [3].

*Corresponding author at: Department of Mechanical Engineering, Bilkent University, Ankara, 06800, Turkey
Email addresses: ege.guven@bilkent.edu.tr (Ege Guven), ykarpat@bilkent.edu.tr (Yigit Karpat), melihc@bilkent.edu.tr (Melih Cakmakci)

5 Additive manufacturing systems that use the VPP approach typically consist of a vertical positioning system, a light source, and a container. The part is built gradually using the vertical positioning system to lower the platform as the polymer resin is cured at the locations where the ultraviolet light is projected. To achieve superior dimensional precision, it is essential to have precise control of the motion of the positioning system and the intensity of the light source, along with an understanding of the material properties of polymer
10 resin. Utilization of a high pixel density DMD chip allows building of micro-scale parts with high accuracy and relatively low cost [4].

In order to prepare the desired part for production, its computer-generated solid model is sliced vertically into layers. These layers are recorded as digital black and white images representing the dimensional features of the part at different heights. These images are then projected on the resin surface during the VPP process
15 so that the part is produced layer-by-layer. In general, there are two ways to project light onto the resin: vector scanning and projection. When using the vector scanning approach, each non-black pixel (point) on the layer image is scanned using a focused light source such as a laser. Once every point on a layer is scanned, the platform is moved vertically, and the curing of the next layer starts [5]. With the projection-based light source approach, an entire layer is cured at once with the help of a light projector or an LCD screen using
20 the layer images [6]. A vat photopolymerization system can be configured in two ways based on the direction of the light projected on the resin. In the top-down configuration, the light projector is placed above the resin vat, and the platform starts from the surface of the resin and descends into the vat. For the bottom-up configuration, the projector screen is set up below the vat, and the platform starts from one layer thickness above the transparent bottom of the vat. The vertical motion of the platform may be advanced in two ways:
25 layer-by-layer and continuous. With layer-by-layer printing, the platform is moved when the production of each layer is finished. In continuous printing, the platform moves continuously, and the projected images are changed in a timed or position-triggered fashion. Continuous printing produces a better surface finish since no layer marks are present. However, the platform's speed must be arranged carefully to avoid undercuring. In this paper a continuous top-down approach has been utilized. Pan et al. developed a method that utilizes
30 the capillary properties of the resin to reduce the stair-step effect between layers caused by layer-by-layer printing and improve the surface finish [7]. However, this method requires a second round of light exposure after the part is removed from the resin, making the process more complex.

In recent years, significant advances in vat photopolymerization have improved the dimensional accuracy of the parts produced. One of the most significant approaches is the utilization of grayscale masks instead of
35 binary, i.e., black and white, masks. In earlier examples in the literature, the grayscale modifications were done manually, graying certain parts of the layer images. For example, in Lee et al. [8], Park et al. [9] and Mostafa et al. [10], researchers improved the resolution of their parts by grayscaling the images they project. These methods are primarily based on trial and error, and their application may not be feasible for improving

parts with more complex geometries. More recently, Zhou et al. used linear programming optimization to
40 reduce boundary errors and achieve sub-pixel resolution [11], [12]. Their method focuses primarily on the
boundaries of the individual layers and employs a simpler curing model for their study. While the proposed
formulation improves the horizontal (XY) resolution significantly, it disregards the errors in the z-direction
and is prone to over-curing if overhanging structures are introduced. Pritchard et al. [13] and Bonada et
al. [14] used grayscale images to reduce *cure-through* in continuous printing. Their correction model only
45 considers the overcuring in the z-direction and does not account for the horizontal irradiation distribution
and its effect on curing. Wang et al. mapped the power density distribution of their projector and used
grayscale to counteract the effects of uneven distribution in large objects [15]. Lichade et al. used grayscale
images with continuous printing to improve the surface quality and reduce the porosity of fabricated parts
[16]. You et al. utilized neural network based machine learning to produce grayscale masks to counteract
50 the effects of light scattering [17]. Dithering effect has been shown to be a viable alternative for achieving
grayscale equivalent layer images in monochromatic systems [18, 9]

Photobleaching is the decomposition of the photoinitiator inside the resin as it cures [19]. Emami et
al. demonstrated the photobleaching effect in photocurable resins and developed a multiphysics model to
address its effects on printed parts [20, 21]. They have also modeled the propagation and attenuation of light
55 within the resin in an effort to increase the dimensional accuracy of Cured VPP parts [22]. Ray tracing was
used to model the irradiation inside the resin by Limaye et al. to be used as part of a VPP layer cure model
[23]. A technique for analytically determining the Jacobs working curve [5] for a photocurable material has
been developed by Li et al. [24]. They used the solid absorbance, liquid absorbance, and gelation time of the
polymer resin to produce an analytical *Jacobs working curve* which agrees with the experimental results with
60 less time and material waste. This robust method for determining the properties of a resin has been used by
many researchers. After the properties of the material and the light source are characterized, the results can
be utilized as a solidification model, predicting the part dimensions given production parameters. Westbeek
et al. developed a multi-physical modelling framework to predict the defects a printed part will have without
the need for a test print [25]. In [26], authors developed a workflow for fabricating micro-needles intended
65 for transdermal drug delivery after parameter optimization based on the design of experiments. Moreover,
the developed solidification model can improve the process by using online or offline optimizations. Li et al.
developed a tunable pre-curing approach to improve fidelity and efficiency in [27] by keeping the resin at a
gelled state during printing. Wicker et al. designed a multiple vat VPP system for building multi-material
parts with a wide variety of materials, resulting in various part functionalities [28]. Tureyen et al. developed
70 an iterative learning controller for improving accuracy in micro-scale vat photopolymerization systems [29]
with the use of a one-dimensional solidification model.

This paper presents a model-based dimensional accuracy improvement method using a voxel-based

grayscale dynamic optimization. In VPP systems, each pixel in the layer images represents the unit volume of the built part, called a *voxel*. During the production, the irradiance of the light beam projected for each pixel is not entirely confined to the targeted voxel, and it lights up a predictable region inside the resin, transferring energy for curing to a larger volume than the targeted voxel. Therefore, the images sent to the projector should be optimized considering the light distribution from all pixels to get a cured object as close as possible to the original CAD model. Although experimental validations for our method are presented using a top-down with continuous motion projection-based system primarily targeting micro-scale parts, our approach is generic enough to be extended to all VPP systems.

The outline for the remaining parts of this paper is as follows. In Section 2, a mathematical model that predicts the solidification process is presented. Section 3 proposes our model-based projection optimization with dynamic programming. In Sections 4 and 5, our experimental vat photopolymerization setup, process parameters, and procedures are given. In Section 6, the optimization method is validated with a detailed example. Lastly, Section 7 discusses our current results and possible future work.

2. Solidification Model

Mathematical models describing the underlying physical mechanisms of a process are developed as a first step to propose calculated improvements. For VPP systems, using mathematical equations to represent the layer-by-layer production of a part involves combining optical and chemical principles with platform motion dynamics. In order to relate the projected image and the platform motion to the part dimensions as the model output, a coordinate system is defined as shown in Figure 1. Here, the resin surface is considered as the $z = 0$ level, and one of the corners of the projected image is taken as the origin with $x = 0$ and $y = 0$.

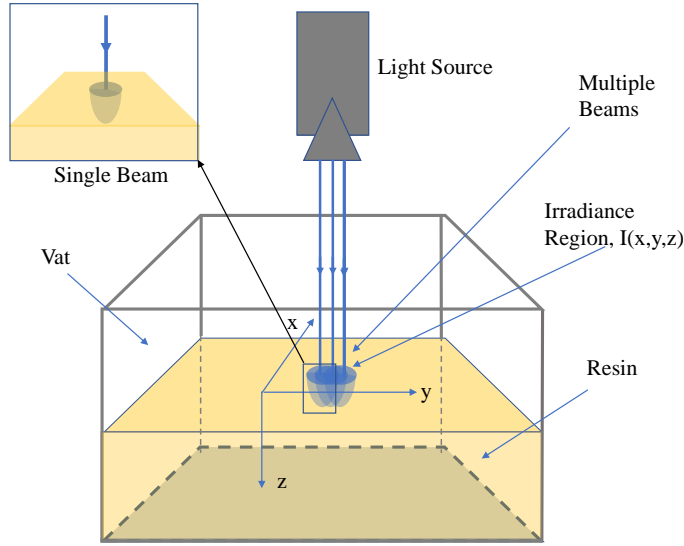


Figure 1: Irradiance of multiple light beams on a photo-polymeric resin surface where calculation by applying superposition of the irradiance single beams is possible.

Understanding the behavior of the light beam as it penetrates the resin is crucial to estimate how the resin will cure when exposed to a layer image from the projector. A projected image can be considered as a collection of light beams entering the resin. For example, in Digital Light Processing (DLP) projectors, the layer image projected on the resin surface comprises pixel lights generated by individual micro-mirrors on the Digital Micro Device (DMD) chip [15]. A model that explains how a single pixel of light behaves in the resin can predict the behavior of a projected image composed of many light beams using the superposition principle.

The absorption of light inside a liquid can be modeled using the *Beer-Lambert Law*:

$$I(z) = I_0 e^{-\mu z} \quad (1)$$

where $I(z)$ is the irradiance at z , I_0 is the irradiance on the resin surface, and μ is a penetration constant. As an alternative to the form presented in Eq.(1) a transmittance function, $T(z)$, can be defined as

$$T(z) = e^{-\mu z} = 10^{-cz} \quad (2)$$

where c is the absorption constant for the liquid.

The Beer-Lambert Law is presented as a one-dimensional relationship applied in the vertical (liquid depth) direction. However, many researchers have observed that the light distribution and absorption profile

in the resin is not a beam shape with uniformly decreasing irradiance (such as [11], [12]), and it somewhat resembles a distorted cone shape, as shown in Figure 1. Therefore, the distribution of light on the resin surface and layers below should be included in the irradiance formulation for more accurate results. The effect of light distribution can be represented in irradiance calculations using a two-dimensional distribution function as shown in Eq.(3).

$$I_0(x, y) = a \cdot e^{-\left(\frac{(x-x_0)^2}{2\sigma_x^2} + \frac{(y-y_0)^2}{2\sigma_y^2}\right)} \quad (3)$$

The equation given in Eq.(3) is a typical Gaussian distribution function with two variables (x, y) with centering parameters (x_0, y_0) and distribution parameters σ_X and σ_Y . In addition, a constant, a , is also introduced to account for the grayscale value of a particular pixel in the layer images projected from the light source. By re-arranging Eq.(1) and Eq.(3), the irradiance from a single pixel of light entering the surface at (x_0, y_0) on a point with the coordinates (x, y, z) can be calculated as shown in Eq.(4)

$$I_{single}(z) = a \cdot e^{-\left(\frac{(x-x_0)^2}{2\sigma^2} + \frac{(y-y_0)^2}{2\sigma^2}\right)} \cdot 10^{-cz} \quad (4)$$

The constants $\sigma = \sigma_X = \sigma_Y$, and c determine the distribution of light in x and y directions respectively and are generally found with experiments. Understanding their effect on the general form of light absorption is necessary for identifying model constants. Analyzing Eq.(4) shows that increasing c reduces the amplitude as it increases the absorption, whereas increasing σ widens the boundaries as it increases the standard deviation of the Gaussian function. The light absorption distribution of multiple pixels can easily be modeled by superposing the single-pixel light distributions centered around each lit pixel, as shown in Figure 1. With the calculation of irradiance of multiple pixel light, a solidification model can be formulated to predict the production results of parts with various shapes.

Before VPP manufacturing, the part's solid model is sliced into k layers, and an image is produced for each layer. A layer is a digitized approximation of a part at a specific height. Assuming uniform thickness for each layer, as the number of layers increases (i.e., $K \rightarrow \infty$), this approximation of the part becomes more accurate. Each of these layer images is shown on the projector screen during manufacturing. In Figure 2, the slicing and layer preparation process of the simple part is shown. The target shape is a hollow square prism, which is first sliced and pixelated for production, and the voxel definitions are formed. When the layer images, which are composed of pixels, are assumed to represent the part's features with a specific thickness, this new unit volumetric area is defined as a voxel. The shape in Figure 2 is sliced in to l layers and represented with $l \times f \times h$ voxels. Each layer with $f \times h$ pixels is shown from the projector to produce the part.

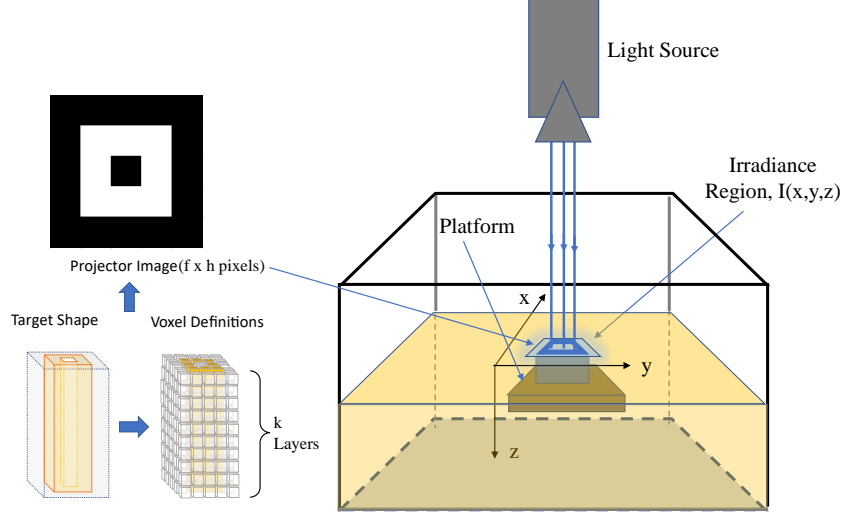


Figure 2: Irradiance of a square layer on a photo-polymeric resin surface.

In order to define the equations of the linear programming problem, the terms source pixel and target voxel need to be defined. Source pixels are the pixels projected onto the resin on each layer. Target voxels are the voxels that are meant to be cured. In Eq.(4), the effect of a single light beam generated from a source pixel on the corresponding layer image is calculated. Then, the total irradiance accumulated at a target voxel can be calculated as the sum of the irradiance from all the source pixels from the same or previous layer images. This value can be calculated by applying Eq.(4) to all layers and pixels with superposition as shown in Eq.(5).

$$I_{(i,j,k)} = \sum_{n=1}^k \sum_{m=1}^f \sum_{l=1}^h a_{(l,m,n)} \cdot e^{-\left(\frac{(i-l)^2}{2\sigma^2} + \frac{(j-m)^2}{2\sigma^2}\right)} \cdot 10^{-c(k-n)} \quad (5)$$

In Eq.(5), (l, m, n) index the (x, y, z) coordinates of the source pixels, and they were introduced to avoid confusion with the target voxel index (i, j, k) . The energy absorbed by a voxel can be calculated by multiplying the total irradiance on that voxel by the exposure time, t (see Eq.(6)).

$$E_{(i,j,k)} = I_{(i,j,k)} \cdot t \quad (6)$$

The energy required to cure the resin is called the critical energy, E_c . If the energy absorbed by a voxel goes above the critical energy, the resin in that voxel cures. In continuous printing systems, the exposure time t is inversely proportional to the speed at which the platform moves vertically. In this system, the platform is lowered into the resin at a speed of $0.03mm/s$. The speed of the platform has been chosen through experimentation, by inspecting the parts printed without optimization and determining at which

speed the parts were most accurate and with least amount of defects. Layer thickness is $0.112mm$, and the time it takes for the platform to move one layer (i.e., the exposure time) is $0.373s$. The platform speed can be reduced to increase the exposure time, which effectively increases the energy absorbed by all voxels. Therefore, for a constant speed system, the energy distribution of any layer with size $f \times h$ can be written in matrix form as Eq.(7).

$$E(k) = t \cdot \begin{bmatrix} I_{(1,1,k)} & I_{(1,2,k)} & \cdots & I_{(1,h,k)} \\ I_{(2,1,k)} & I_{(2,2,k)} & \cdots & I_{(2,h,k)} \\ \vdots & \vdots & \ddots & \vdots \\ I_{(f,1,k)} & I_{(f,2,k)} & \cdots & I_{(f,h,k)} \end{bmatrix}_{f \times h} \quad (7)$$

Compiling the energy matrices for all layers into a 3D matrix gives the energy distribution model for a part. By comparing the elements of the energy matrices to the critical energy, E_c , the voxels that are cured can be identified, and the solidification model can be presented.

3. Model Based Process Optimization with Dynamic Programming

Once a solidification model with specific parameters and variables is developed, improvements can be identified so that the manufacturing process can be performed better (for example, faster production with better quality). For complex systems and processes that have many variables, formulating and solving an optimization problem is a typical approach for finding a set of settings with the optimal performance. For most manufacturing processes, the objective is to minimize an accumulated error representing the deviation from the intended production properties. The solidification model developed in the previous section represents the basis for the problem constraints. Our target is to utilize grayscaling, which reduces the irradiance of light on a localized area, to reduce the accumulated error in manufacturing.

Following the same notation from before, Eq.(5) can be rewritten in the form

$$I_{(i,j,k)} = \sum_{lmn} a_{(l,m,n)} \cdot w_{(i,j,k,l,m,n)} \quad (8)$$

where w are irradiance model coefficients of the source pixels. Using Eq.(8), the energy absorbed by a voxel at the coordinates (i, j, k) is defined in terms of a and w as Eq.(9).

$$E_{(i,j,k)} = t \cdot \sum_{lmn} a_{(l,m,n)} \cdot w_{(i,j,k,l,m,n)} \quad (9)$$

Each source pixel has a grayscale value g between 0 and 255, 0 representing black (no light) and 255

160 representing white (i.e., full intensity). Grayscale factor a of a pixel is defined as Eq.(10).

$$a = 3 \cdot \left(\frac{g}{255} \right)^\gamma \quad (10)$$

Value of γ will be determined experimentally. The pixel grayscale factor, a , is the design variable of our optimization problem. The objective function, $J(\mathbf{a})$, is the total energy absorbed by all boundary voxels as shown in Eq.(11). Boundary voxels are voxels next to target voxels and are intended to remain uncured.

$$J(\mathbf{a}) = \sum_{d=1}^D E_d(\mathbf{a}) \quad (11)$$

where D is the number of boundary voxels and \mathbf{a} is the vector containing the grayscale factor values for all source pixels. E_d is the energy absorbed by a boundary voxel.

The formulation for the grayscale optimization problem can be written as shown in Eq.(12).

$$\min_{\mathbf{a}} J(\mathbf{a}) \text{ such that } \begin{cases} \mathbf{A} \cdot \mathbf{a} \leq \mathbf{b} \\ \mathbf{lb} \leq \mathbf{a} \leq \mathbf{ub} \end{cases} \quad (12)$$

where \mathbf{lb} and \mathbf{ub} are the lower and upper bound of values elements of \mathbf{a} can have. The goal of the optimization is to minimize the objective function $J(\mathbf{a})$ while keeping the energy values of target voxels above the critical energy. This allows the part to be built with high accuracy, using as little energy as possible.

170 When the target voxel located at (i, j, k) needs to cure as part of the production, the inequality constraint given in Eq.(13) must be satisfied.

$$E_{(i,j,k)} \geq E_c \quad (13)$$

For successful production of a part, each target voxel needs to cure when the process finishes. This collection of constraints can be represented in our formulation by calculating a matrix \mathbf{A} , each row of which can be written as shown in Eq.(14).

$$\mathbf{A}_r = \mathbf{A}_{(i,j,k)} = -t \cdot [w_{(i,j,k,1,1,1)} \ w_{(i,j,k,1,1,2)} \ \cdots \ w_{(i,j,k,1,3,n)} \ \cdots \ w_{(i,j,k,l,m,n)}]_{1 \times q} \quad (14)$$

175 \mathbf{A} is a $p \times q$ matrix where p is the number of inequality constraints (i.e. the number of target voxels), and q is the number of variables (i.e. the number of source pixels). Each row of \mathbf{A} has a corresponding value in vector \mathbf{b} with p elements (see Eq.(15)).

$$\mathbf{b}_r = [b_{(i,j,k)}] = -E_c \quad (15)$$

Note the minus sign in Equations Eq.(14) and Eq.(15), since the optimization formulation needs to be a \leq inequality; both sides of Eq.(13) are multiplied by -1 to reverse the sign.

180 Because of the large number of linear relationships existing in the model developed in Eq.(1)-Eq.(7) and considering the vast availability of tools in literature, our optimization problem is formulated as a linear programming problem. After the objective function and the constraint equations are formulated, Matlab Optimization Toolbox is used for solving the actual optimization problem.

185 The formulation of the optimization problem and remapping of the results to slice image form is summarized in the workflow shown in Figure 3.

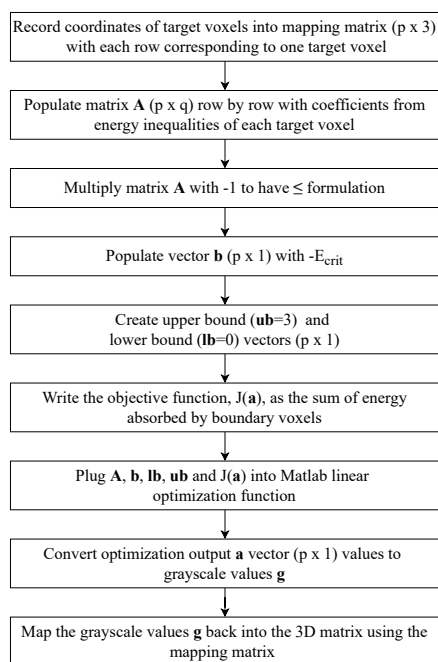


Figure 3: Optimization flowchart explaining the steps followed to optimize any part to be built.

An example of optimizing a simple part is provided in Appendix A to help understand the optimization process.

In an ideal case, all pixels on all the images would be sources, and every voxel in the CAD part would be a target. However, typically, there are computational limitations. Choice of targets and sources along with 190 some basic techniques to improve the computational efficiency of the problem are explained in Appendix B.

4. Experimental Setup

The overall schematic of the rapid prototyping machine used in this study is given in Figure 4. The layer images are sent to the DLP projector in coordination with a precision positioning system that moves the platform using a workstation computer.

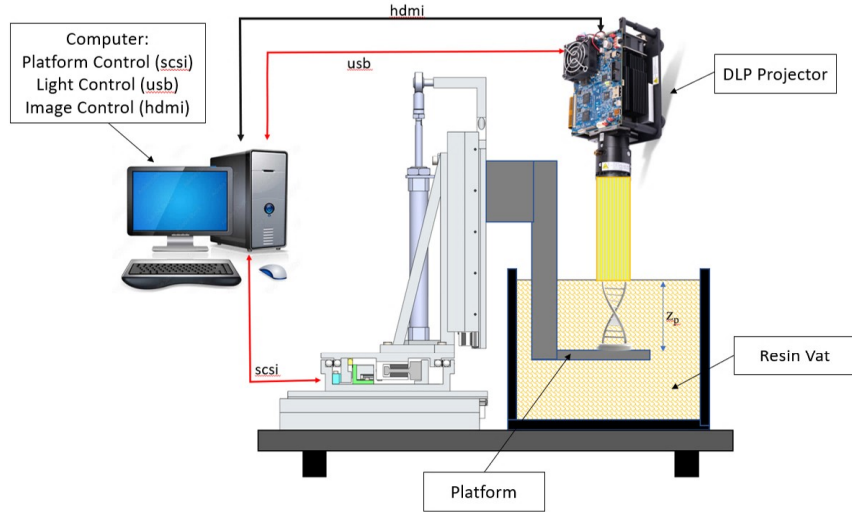


Figure 4: Photograph of the overall rapid prototyping system and its schematic. The Build chamber is enclosed in red glass to avoid curing of the resin from outside light sources.

195 The list of equipment and materials used to build and analyze a part are given in Table 1. Optimization is performed on a separate computer running a Ryzen 5 3600 processor with 64 GBs of DDR4 ram.

No:	Equipment / Material	Brand / Model
1	Positioning System and Controller	Aerotech A3200
2	Projector	Texas Instruments DLP4710EVM
3	Computer	Intel Xeon W3503 Workstation
4	Microscope	Keyence VHX-1000
5	High speed microscope	Keyence VW-9000
6	Scanning Electron Microscope	FEI Quanta 200 FEG ESEM
7	Polymer Resin	Uniz zSG Amber

Table 1: Equipment and material list.

Pixel pitch of the DMD chip is $5.4\mu m$ and the projected pixels are $11.2\mu m$ squares. Further information of the light source can be found in the projector datasheet [30]. Absorption levels of various resins were examined using a Cary 100 spectrometer. The polymer resin used in all experiments is the *zSG Amber* by 200 Uniz. After comparison with alternatives, *zSG Amber* has relatively high absorption near the visible blue light wavelength, between $400 - 450nm$ as shown in Figure B.23.

The process for building a part begins with drawing the part in CAD software. The part is then sliced into layer images. The optimization process modifies the layer images. The layer images are then turned into a video using editing software. The video is projected onto the resin surface while the platform is 205 continuously lowered into the polymer resin vat. At the end of the video, the light from the projector is

switched off, and the platform is raised above the resin. The built part is retrieved from the platform and is cleaned with isopropyl alcohol. Finally, the part is placed into a UV light bath for 5 minutes to be fully cured. The cured part is measured and photographed using the Keyence VHX-1000 microscope. A scanning electron microscope is used if higher accuracy measurements or better images are needed.

210 **5. Identification of Parameters in the Solidification Model**

The formulations given in Eq.(1)-Eq.(7) have various parameters that need to be identified before the solidification model is finalized. Controlled experiments were performed using our experimental setup shown in Figure 4.

215 The model parameters were determined by performing a series of experiments. First, the image shown in Figure 5 was projected onto the resin, and the light inside the resin was photographed from the side with a high-speed camera. Using a picture editing software, the pixels of this photograph with the highest light value of 255 were isolated. The plot formed by the boundary of these pixels was then compared to light distribution model results to fine-tune the constants, where the constants were determined as $c = 0.008 m^{-1}$ and $\sigma = 13$. The images from this process can be found in Figure 6.



Figure 5: Image projected for the calibration of constants. Lit areas have 100%, 75%, 50% and 25% of the maximum light value 255, respectively.

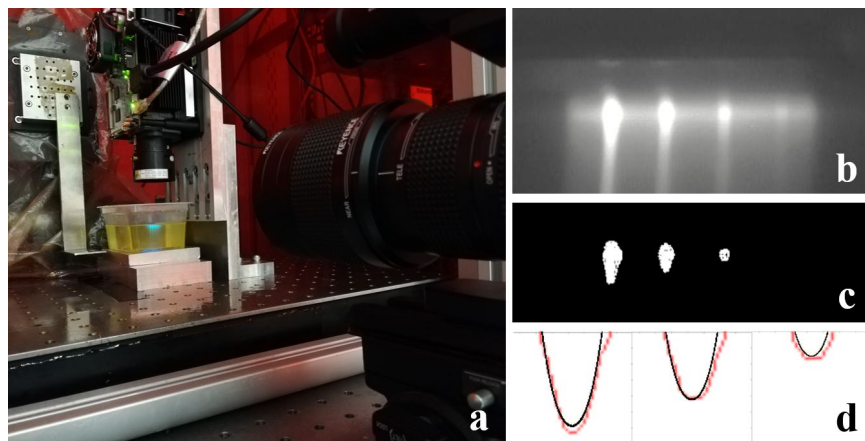


Figure 6: (a) Experiment setup with the high-speed camera directed at the resin vat as Figure 5 is projected onto the resin. (b) High-speed microscope image of light propagation in the polymer resin when Figure 5 is projected onto the surface. (c) Every pixel except those with value 255 has been omitted from A to be able to clearly distinguish the boundaries of a common energy value. Threshold value choice is arbitrary and could have been a value other than 255. (d) After examining how each variable in the model affects the curve's profile, the best set of variables has been chosen depending on how well they fit the experimental curves. Red lines are the experimentally acquired curves, and black lines are the numerical model.

220 Variables that are optimized for this study are the a values given in Eq.(5). Each source pixel has an a value for the amplitude of the Gaussian in the model, and these values depend solely on the grayscale value of the pixel. The energy absorbed by each pixel is a function of \mathbf{a} , the vector containing the a values of all source pixels. Therefore the optimization is formulated around \mathbf{a} . The grayscale values g were not used directly in the formulation in order to lower the computational load on the optimization process. \mathbf{a} is a vector with elements valued between 0 and 3 and is related to the tone values of the pixels g (values between 0 and 255). As defined previously in Eq. (10), these values are related as in the equation in Figure 7. The value of γ was determined experimentally. From the three data points of 100%, 75% and 50% g and their corresponding a values, and also noting the plot starts from the origin, using Eq.(10) with $\gamma = 2.4040$ produces the curve that best fits the data, as can be seen in Figure 7.

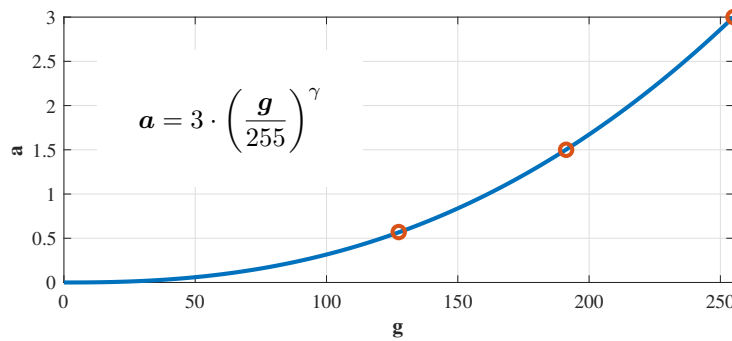


Figure 7: Plot of g vs a . Orange colored dots are the data points.

230 After selecting the constants that best fit the light penetration images, the *dot test* was performed: The platform was fixed at $1mm$ below the resin surface, and a 50×50 pixel square was projected for 60 seconds. The results obtained were compared to the numerical model prediction, and the choice of constants was validated. The methodology used for determining and calibrating the model parameters includes the effect of photobleaching since, cured parts are used along with the light profiles in the resin. It is important to note that the effect of photobleaching on the resin used in this study is relatively low in the wavelength range of the projector ($444 - 465nm$). Figure 8(a) shows the resulting built 3D part from this test. The yellow parabolic overlay is what the model calculated with the chosen constants.

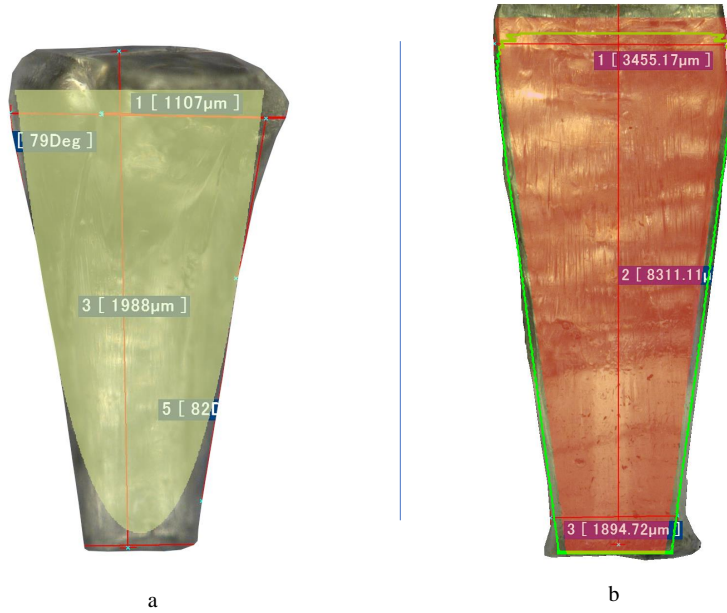


Figure 8: (a)Dot test result. The dome-like structure at the top is formed by the curing of resin pooled on top because of the capillary forces. This phenomenon occurred because the platform was stationary and would not occur in a regular process. (b) Test piece to help determine the critical energy. The red silhouette is the original CAD of the part. The green outline is the prediction of the model for this part.

As explained earlier in Section 2, the solidification model creates a 3D matrix containing values corresponding to the total energy each pixel absorbs during the print. After identifying the speed, a square prism tapered towards the bottom was built. This part is chosen intentionally so that a possible over-curing in print can be observed. In Figure 8(b), the red silhouette is the original part, the green outline is what the model predicted for the built product, and the piece in the background is the built part. The curing threshold value (critical energy) was determined by checking which isoline fits the built part. The green outline in Figure 8(b) was the closest to the built part. Therefore, this energy value was determined as the critical energy.

6. Validation of the Optimization Method

The method outlined in the previous section promises significant improvements regarding the shape of the resulting part after model-based image layer optimization. To test these improvements, a popular benchmark part shown in Figure 9 was manufactured using the optimization of projected images discussed in the previous section. The same part was also built without the optimization to compare how well it works and to validate its feasibility for practical components. Optimization and print results for a relatively simpler part has been provided in Appendix C.

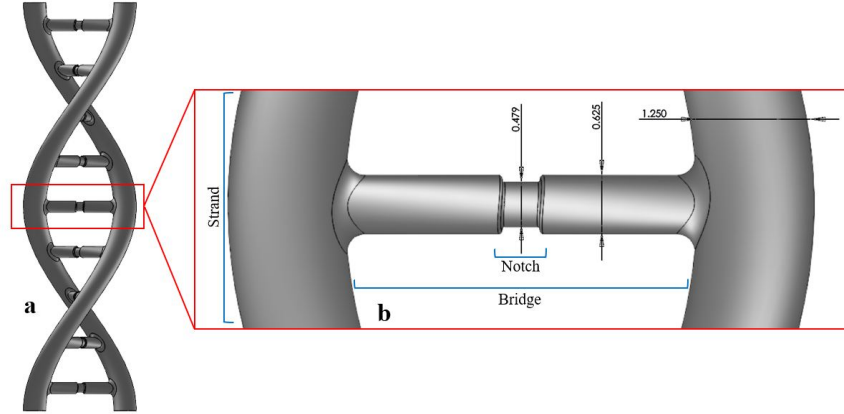


Figure 9: (a) CAD model of a DNA double helix part. (b) The closeup of a single nucleotide bridge section. Dimensions are in mm.

The *DNA double helix part* shown in Figure 9 is selected to test the real-life challenges of additive manufacturing as the nucleotide bridges in DNA allow for the common curing defects such as over-curing and thickness inaccuracy in overhanging structures. Since the feature repeats itself, our validation study focuses on optimizing a single section with one nucleotide bridge to speed up the computations and the manufacturing process. The results of this study can still be used for the whole part because the bridges are far enough apart that their effect on each other is negligible. The notch in the middle of the bridge in the CAD model adds complexity to the part to be produced, testing the capabilities of the proposed optimization method.

The accuracy of the model should be validated before moving on with the optimization. To compare the print simulation and the actual print, the DNA was simulated and printed with no alterations to its layer images. Images of the simulated part and the print are given in Figure 10. The 3D model is obtained as a Matlab volume graph by using the voxels that are identified as cured in the solidification model. The profile of the thinner middle section and the general dimensions of the simulation closely resemble those of the built part. The model accurately predicts how the final built is going to appear when the determined printing parameters are used.

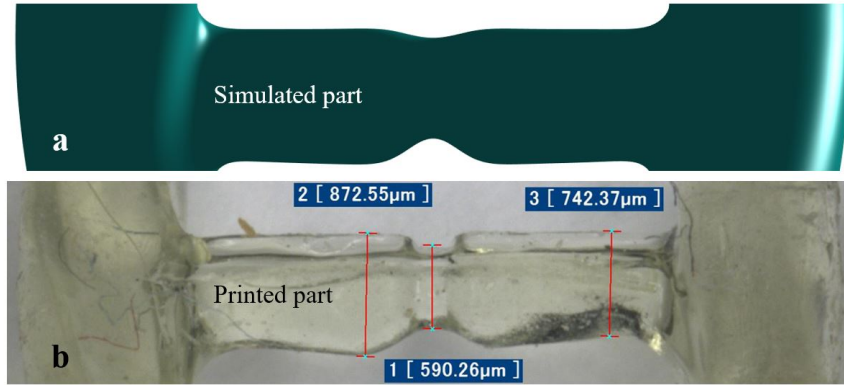


Figure 10: (a) Numerical model of a nucleotide bridge of a DNA molecule. (b) The print result of the same part.

In order to rapidly estimate the benefit of the optimization method, the mathematical model developed in Section 2 is used to simulate the manufacturing process with and without the optimization of the layer images. These simulation results are presented in Figure 11 and Figure 12. Figure 11(b) and Figure 11(c) show how the built part is expected to come out without and with the layer optimization, respectively. The prediction before the optimization in Figure 11(b) shows over-curing on the underside of the bridge. With optimization, this problem has been fixed, and the top part of the notch section became more defined. Figure 12 shows the simulation results from the top, where a slight reduction in the bridge thickness observed in Figure 12(b) is reduced after optimization as shown in Figure 12(c). The simulation results suggest an 11% decrease in the overall volume of the considered DNA section, going from $7.5mm^3$ to $6.7mm^3$.

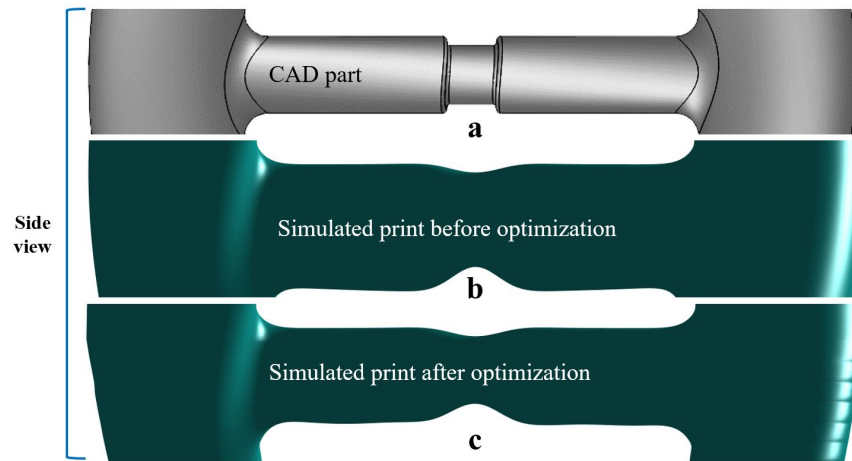


Figure 11: (a) Side view of the DNA section CAD model. (b) Side view of the print simulation before optimization. (c) Side view of the print simulation after optimization.

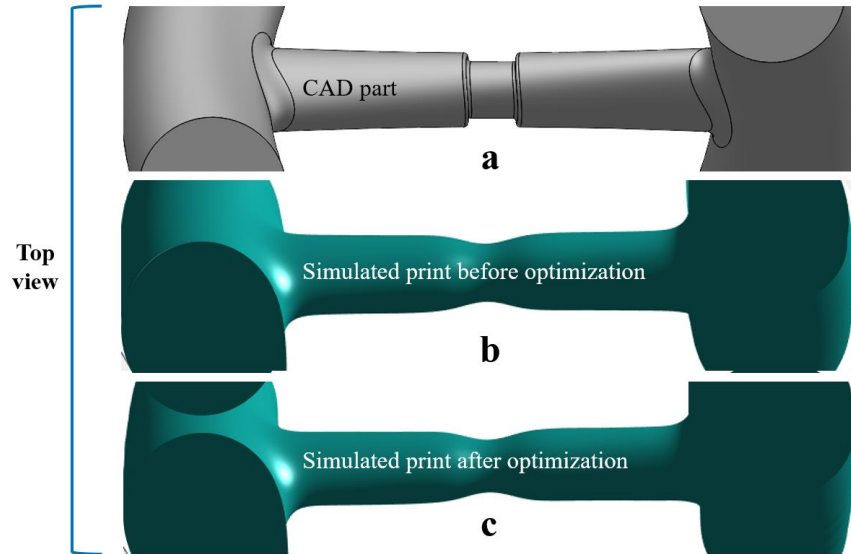


Figure 12: (a) Top view of the DNA section CAD model. (b) Top view of the print simulation before optimization. (c) Top view of the print simulation after optimization.

The predicted simulation results show promising improvements as shown in Figure 11 and Figure 12. Therefore, actual benchmark parts are produced in the VPP machine to verify if the predicted benefit in simulations is obtained. Figure 13 and Figure 14 show how the benchmark part is built before and after the optimization, respectively. Without the optimization, the part is overall thicker than it is supposed to be, the bottom profile of the bridge is distorted with a significant increase in thickness near the notch, and the top side of the connection between the bridge and the main strands is sharper. The thickness in the optimized part is much closer to the original CAD model shown in Figure 9, with the thickness of the notch in this specific example being 495 microns after optimization, 590 microns without the optimization as compared to the 479 microns from the targeted CAD drawing. The bottom profile was straightened out, and the bridge to main strand connections was smoothed out.

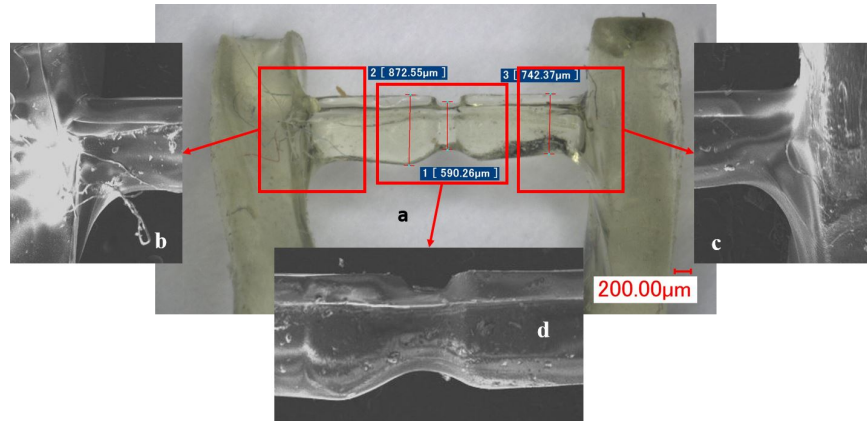


Figure 13: (a) Side view of print of the DNA section before optimization. (b) The E-SEM image close up of the left bridge-strand connection. (c) The E-SEM image close up of the right bridge-strand connection. (d) The E-SEM image close up of the middle section.

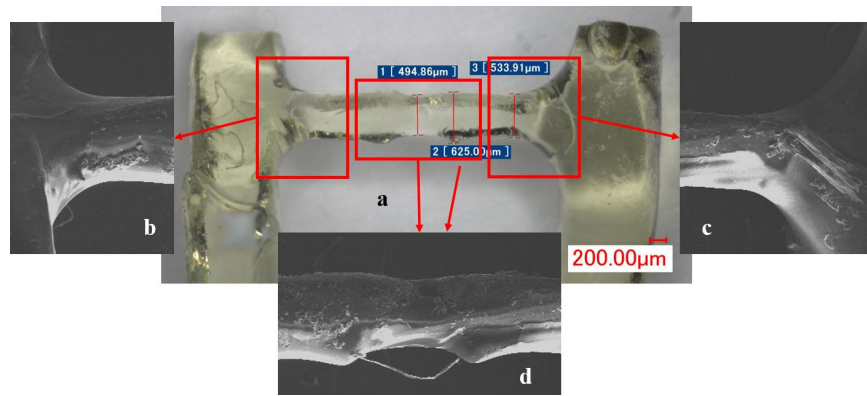


Figure 14: (a) Side view of optimized print of the DNA section. (b) The E-SEM image close up of the left bridge-strand connection. (c) The E-SEM image close up of the right bridge-strand connection. (d) The E-SEM image close up of the middle section.

The grayscale images of the parts were obtained using the environmental scanning electron microscope (E-SEM) mentioned in Section 4. Figure 15 shows the built parts from the top in detail using an SEM. When built parts are observed from the top, the improvement caused by the optimization can be clearly
 290 seen. The overall profile was improved noticeably on both sides, and the sharp-edged sections on the top (middle in this image due to it being the top view) of the part were smoothed out by the optimization.



Figure 15: (a) Top E-SEM view of the DNA section before optimization. (b) Top E-SEM view of the optimized DNA section.

Figure 16 and Figure 17 show how two layers of the part were changed by the optimization. The layer considered in Figure 16 is from the underside of the bridge. Optimization darkened the middle section around the notch. This means that the energy absorbed from the upper layers' projection is enough to cure the middle section for this and the following layers. Notice that the section of the bridge just before connecting to the main strand is lit. This is important as it is a clear example of how optimization solves issues in the part. In Figure 13, the underside profile of the bridge is thinner closer to where the bridge connects to the strands and gets thicker towards the middle. Since the overall structure is thicker and needs to be thinned down, these connections are at the risk of becoming too thin. To offset the excessive thinning in these areas, the optimization left the parts of the layer image that correspond to these areas lit while darkening the middle section. This results in the problematic areas absorbing more energy and having more voxels cured, in turn achieving a more uniform shape with an accurate thickness, as can be seen in Figure 14. Layer in Figure 17 is from the middle of the bridge. There is slight graying or blacking out of regions, making the final shape thinner. Notice in both cases, the image is no longer symmetric after optimization. The helical structure of the DNA causes the parts that end up underneath the strands to overcure. Likewise, the opposing sides are more prone to undercuring. Therefore, parts of the images that correspond to the bottom sides of the strands are darker after optimization.

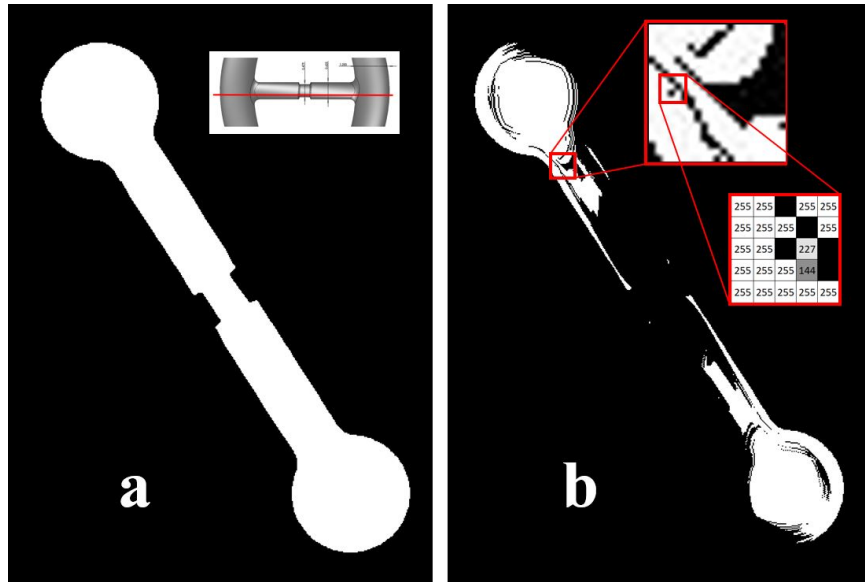


Figure 16: (a) A projected layer image near the bottom of the bridge, before optimization. Image on the top right shows where in the part this layer is located. (b) Image of the same layer after optimization.

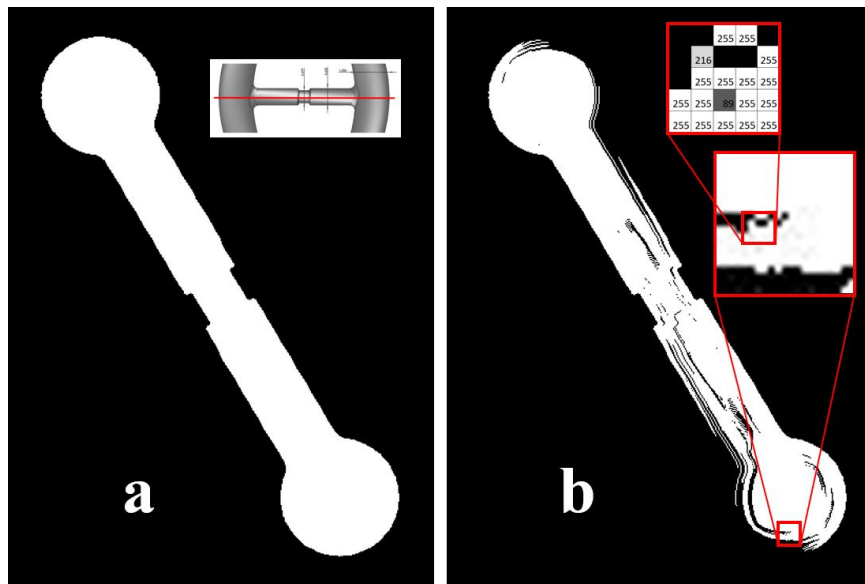


Figure 17: (a) A projected layer image at the middle of the bridge, before optimization. Image on the top right shows where in the part this layer is located. (b) Image of the same layer after optimization.

The simulation results show that there is a 24.7% decrease in the number of overcured voxels due to the optimization. A more robust selection of sources can decrease the overcured voxel count further, as described in [Appendix B](#).

Multiple parts were built with and without optimization, and notch thickness values were averaged. The average notch thickness before the optimization is 587 microns with a standard deviation of 72.3. For parts

built without optimization, measured values along with their average and the target dimension is given in Figure 18(a). The average notch thickness after optimization is 476 microns with a standard deviation of 29.5. For optimized parts, measured values along with their average and the target dimension is given in Figure 18(b).

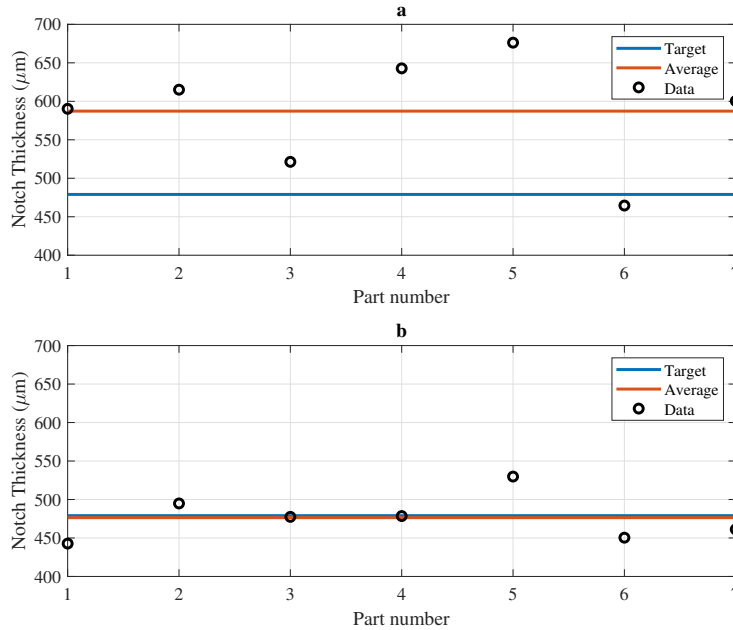


Figure 18: (a) Notch thickness values for parts built without optimization. (b) Notch thickness values for optimized built parts. Blue line is the targeted dimension, black dots are the measured notch thickness values and orange lines are the averages of the measured values.

Figure 18 shows that the optimization not only improved the dimensional accuracy of the part and it also reduced the variance in the data set.

7. Conclusions and Future Work

This paper presents a dynamic optimization scheme for improving the dimensional accuracy of parts built using continuous micro vat photopolymerization. Irradiation of light from layer image pixels is mathematically modeled and used to estimate which areas of a 3D part would be cured during an VPP process. Using this model, the layer images are optimized with grayscaleing to produce the closest possible print result to the initial CAD drawing of the part. As a result of this optimization, the simulation result is that the number of overcured voxels was reduced by 24.7%. Multiple built parts with and without optimization show that the average notch thickness without optimization is 587 μm while with optimization, it drops to 476 μm , a value much closer to the desired 479 μm . The optimization also reduced the standard deviation significantly, resulting in a printing method that is both more accurate and more precise.

Micro-scale parts are very prone to overcuring around and under overhanging features. The proposed
330 method allows precise dimensional tuning for micro-scale parts through independent grayscaling of each
pixel. Energy absorbed by every pixel is closely regulated to prevent excess light exposure during the print.

The success of this micro vat photopolymerization based approach can also be utilized in larger-scale
objects if certain computational limitations are overcome. Future work includes improving the efficiency
of modeling and optimization calculations and the addition of more features from the VPP process to our
335 methodology.

Appendix A. Simple Example

In Section 2, a mathematical solidification model for the VPP process was presented. In Section 3, this
model was used to improve the dimensional accuracy of the printing process by use of linear programming
optimization techniques. The VPP process utilizes multiple layer images represented in terms of matrices
340 in the formulations. Typically, these matrices and vectors are too big to present on paper, even for a simple
part.

In order to give an outline of how the optimization problem is formulated and the energy and grayscale
values are affected during the optimization, an example of a 5-pixel diameter cylinder with a height of 5
layers will be provided here.

345 The object is broken into voxels as seen in Figure A.19(a). The cylinder 5 layers in height and 5 pixels
in diameter is assumed to be contained in a volumetric box of $7 \times 7 \times 5$ voxels. Since the cylinder has a
uniform cross-sectional area, the layer image is the same for all layers. It is important to note that although
the cylinder has a perfectly circular cross-section, the layer image shown in the projector will be imperfect
with a pixelated version. The more pixels used, the better the quality of the image. Figure A.19(b) shows
350 the target voxels and the boundary voxels used for a layer during optimization.

do not affect the energy absorbed by the voxel; therefore, their values are set to zero. The only source with the value -1 is the source pixel that is coincident with the chosen voxel. Afterwards \mathbf{b} , \mathbf{ub} , \mathbf{lb} and $E(\mathbf{a})$ are calculated. \mathbf{b} and $E(a)$ are calculated through Eq.(15) and Eq.(11) respectively. For this example, the critical curing energy E_c was taken to be 170. \mathbf{ub} and \mathbf{lb} are the same in all versions, as values of \mathbf{a} are between 0 and 3.

$$\mathbf{b} = \begin{bmatrix} -170 \\ -170 \\ \dots \\ -170 \\ -170 \end{bmatrix}_{105 \times 1} \quad (\text{A.2})$$

The optimization is performed, and the \mathbf{a} vector containing the a values for all source pixels is obtained. This vector is transformed into the \mathbf{g} vector using Eq.(10) and new images are constructed by mapping the values of the \mathbf{g} vector back to the corresponding pixels. The result of this process is given on the right column of Figure A.20.

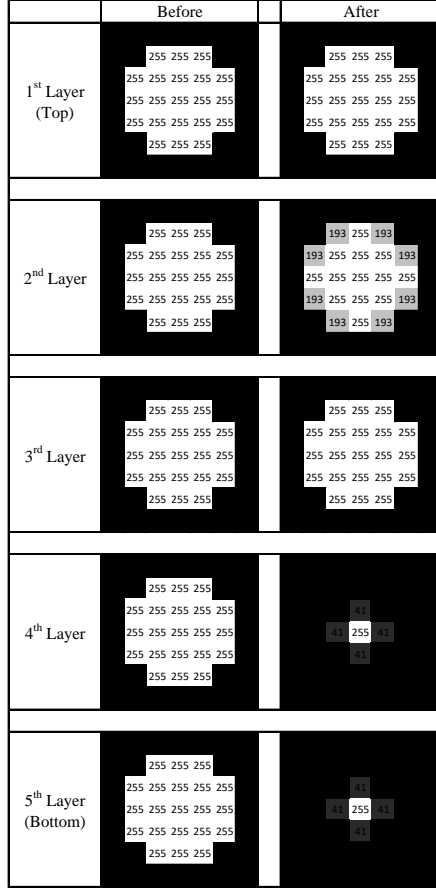


Figure A.20: Light value of each projected pixel, before and after optimization.

Notice that the optimization algorithm greys parts of the 2nd Layer, but the 1st and 3rd Layers receive full exposure. In the proposed optimization procedure, the few layers at the top of any part needs full exposure as the light from a few layers is not enough to cure the desired voxels. This dictates how the target voxels are selected. Voxels that need to be cured are selected as targets if they receive more energy than E_c in the simulation without optimization. Since the underexposed voxels are not designated as targets, the optimization algorithm can occasionally decrease the light at top layers slightly even though ideally it should be full exposure for the best overall result. Therefore, the topmost layers of a part may not be accurate. This issue will be addressed in future work.

In Figure A.21, the energy absorbed by the voxels in the third layer before and after optimization is given. The third layer was chosen because the top layers usually cannot get enough energy to go above the critical energy, and the lower layers produce very similar results and do not add anything of significance to the discussion. Following the color pattern from Figure A.19, voxels marked yellow go above the critical energy and are thus cured. White voxels absorb less energy than critical energy and remain uncured. Having

380 voxels that should not be cured marked yellow means an over-curing problem in those voxels.

3 rd Layer													
174	177	178	179	178	177	174	164	166	168	168	168	166	164
177	180	181	182	181	180	177	166	169	170	170	170	169	166
178	181	183	183	183	181	178	168	170	172	172	172	170	168
179	182	183	184	183	182	179	168	170	172	173	172	170	168
178	181	183	183	183	181	178	168	170	172	172	172	170	168
177	180	181	182	181	180	177	166	169	170	170	170	169	166
174	177	178	179	178	177	174	164	166	168	168	168	166	164

Figure A.21: Energy absorbed by each voxel in the third layer, before and after optimization.

The simulation suggests that using the layer images produced by the optimization algorithm fixes the overcuring issue and ensures the curing of only the intended voxels.

Appendix B. Sources, Targets and Segmentation

Ideally, all pixels would be sources, and all voxels of the CAD part would be targets. However, each source adds an extra variable to be optimized. Increasing the number of sources or targets enlarges the matrices put into the optimization algorithm. If these matrices become too large, the computational power required becomes immense.

The memory capacity of the computer performing the optimization can be a serious bottleneck in terms of the number of variables that can be optimized at once. Depending on the size of the part, it may not be possible to optimize all pixels and voxels at once. This makes the choice of sources and targets crucial. Since over-curing is a more prevalent issue than under-curing, only the lit pixels in the layer images were chosen as sources. The coincident voxels that absorb more energy than the critical threshold with unedited images are selected as the targets.

If there are still too many variables after the choice of targets and sources, the part is divided into small segments to be optimizable. Steps followed in how a part is divided into segments are shown in the flowchart in Figure B.22.

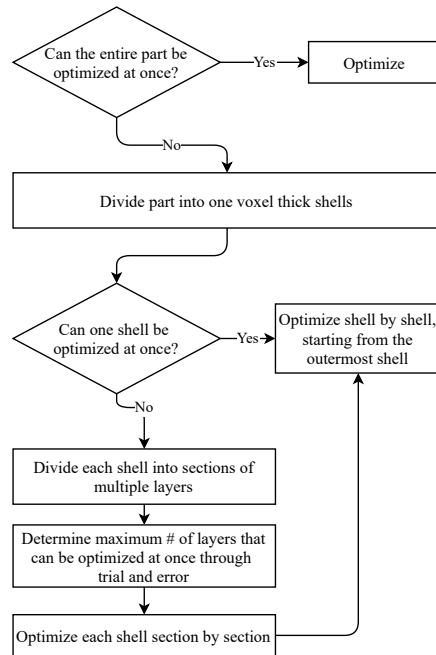


Figure B.22: Segmentation flowchart.

The part is first split into shells. These shells fit into each other and make up the 3D part, much like the layers of an onion. Those shells are then split into sections of multiple layers to lower the computation load. In the case of the DNA part example, 30 layers were used. The 30 layer sections have 50% overlap, meaning every single layer is part of two adjacent segments. (Section1: layers 1-30, Section 2: layers 16-45 ...) Increasing the overlap of the sections result in a more uniform optimization result. This overlap decreases the error caused by the segmentation by 18%.

It is also important to check the polymer spectroscopy during the troubleshooting of problems such as undercuring or overcuring. Figure B.23 shows the spectroscopy results for the polymer resin used in our experiments.

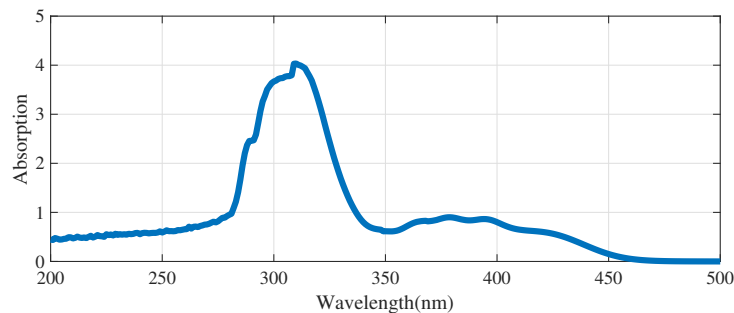


Figure B.23: 200-500 nm spectroscopy results for the polymer resin. The small hill around 400nm allows for the curing of the resin in the visible light range.

Appendix C. Simple part with overhang

A simple part with a 45° overhang was simulated and printed first without any alterations, and then again after the layer images had been optimized. The CAD drawing of The part is given in Figure C.24(a). Figure C.24(b) shows the improvement caused by the optimization by comparing the simulations with and without the optimization. Red areas depict the areas that would have been overcured if the optimization had not been performed.

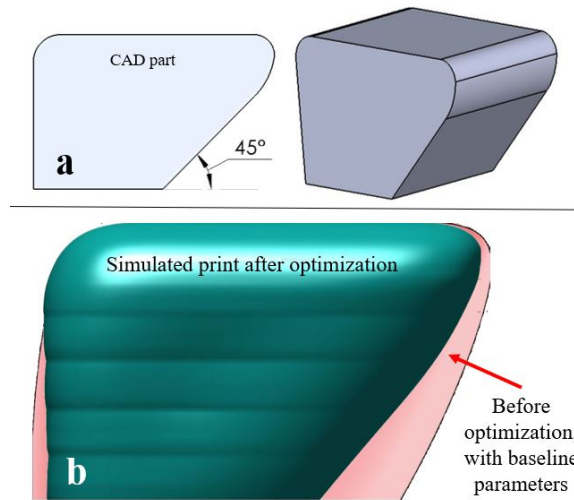


Figure C.24: (a) Side and isometric CAD view of a simple part with an overhang. (b) Simulated improvement on the print accuracy. Green part is the simulated result after optimization, red area is the predicted overcuring without the optimization.

The print results are presented and compared with the simulated parts in Figure C.25.

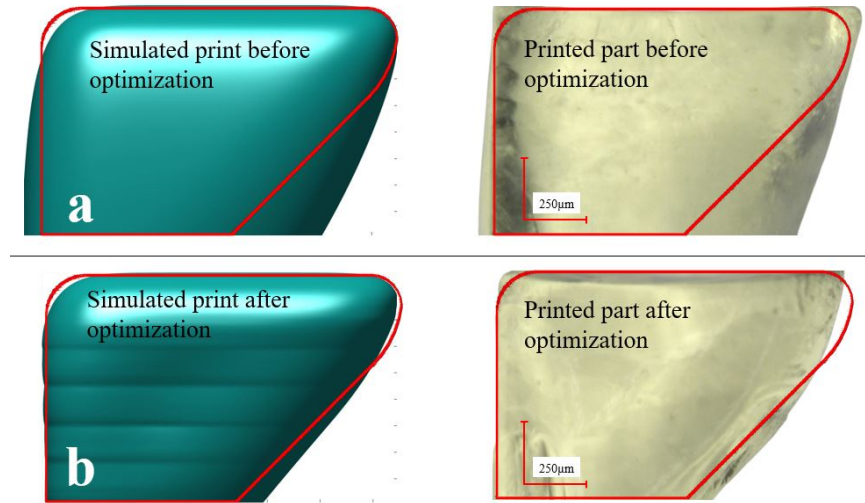


Figure C.25: (a) Print simulation (left) and the print result (right) of the part without optimization. (b) Print simulation (left) and the print result (right) of the part with optimization. The red outline is the perimeter of the cad drawing and represent the intended profile for this print. The horizontal lines seen on the optimized simulation are a result of the segmentation. They do not have a considerable effect on the final print, evidenced by their absence on the printed part.

Along with the model simulation being accurate in estimating how a print will turn out, the optimization has improved the part accuracy significantly. The overcuring under the overhang and on the left side of the part was reduced. Sizes of the overcured areas under the slope for the simulations and the printed parts are given in table C.2.

Overcured area under the slope (mm^2)	Simulation	Print
Before Optimization	19.1×10^{-2}	23.5×10^{-2}
After Optimization	4.5×10^{-2}	5.6×10^{-2}

Table C.2: Area under the slope that is overcured with respect to the intended CAD of the part.

ACKNOWLEDGMENTS

The equipment used in this research was partly sponsored by the Scientific and Technical Research Council of Turkey (TUBITAK), Project No: 113M172. [‘Development of a Multipurpose Micro Manufacturing System using Modular and Iterative Learning Control Algorithms’]

References

- [1] F. Zhang, L. Zhu, Z. Li, S. Wang, J. Shi, W. Tang, N. Li, J. Yang, [The recent development of vat photopolymerization: A review](#), Additive Manufacturing 48 (2021) 102423. doi:<https://doi.org/10.1016/j.addma.2021.102423>.

URL <https://www.sciencedirect.com/science/article/pii/S2214860421005753>

- [2] W. Gao, Y. Zhang, D. Ramanujan, K. Ramani, Y. Chen, C. B. Williams, C. C. Wang, Y. C. Shin, S. Zhang, P. D. Zavattieri, [The status, challenges, and future of additive manufacturing in engineering](#), *Computer-Aided Design* 69 (2015) 65–89. doi:<https://doi.org/10.1016/j.cad.2015.04.001>.
URL <https://www.sciencedirect.com/science/article/pii/S0010448515000469>
- 430 [3] E. MacDonald, R. Wicker, [Multiprocess 3d printing for increasing component functionality](#), *Science* 353 (6307) (2016) aaf2093. doi:[10.1126/science.aaf2093](https://doi.org/10.1126/science.aaf2093).
URL <https://www.science.org/doi/abs/10.1126/science.aaf2093>
- [4] M. Vaezi, H. Seitz, S. Yang, A review on 3D micro-additive manufacturing technologies, *The International Journal of Advanced Manufacturing Technology* (2013). doi:[10.1016/j.addma.2019.100889](https://doi.org/10.1016/j.addma.2019.100889).
- 435 [5] P. F. Jacobs, [Fundamentals of Stereolithography](#), in: 1992 Int. Solid Free. Fabr. Symp., no. July, 1992, pp. 196–211. arXiv:[arXiv:1011.1669v3](https://arxiv.org/abs/1011.1669v3), doi:[10.15781/T24M91T5H](https://doi.org/10.15781/T24M91T5H).
- [6] A. S. Limaye, [Design and Analysis of a Mask projection Micro Stereolithography System](#), Ph.D. thesis, Georgia Institute of Technology (2004).
URL <http://eprints.uanl.mx/5481/1/1020149995.PDF>
- 440 [7] Y. Pan, X. Zhao, C. Zhou, Y. Chen, Smooth surface fabrication in mask projection based stereolithography, *J. Manuf. Process.* 14 (4) (2012) 460–470. doi:[10.1016/j.jmapro.2012.09.003](https://doi.org/10.1016/j.jmapro.2012.09.003).
- [8] D. Lee, T. Miyoshi, Y. Takaya, T. Ha, 3D Microfabrication of Photosensitive Resin Reinforced with Ceramic Nanoparticles Using LCD Microstereolithography, *Journal of Laser Micro/Nanoengineering* (2006). doi:[10.2961/jlmm.2006.02.0011](https://doi.org/10.2961/jlmm.2006.02.0011).
- 445 [9] I. B. Park, Y. M. Ha, S. H. Lee, Dithering method for improving the surface quality of a microstructure in projection microstereolithography, *International Journal of Advanced Manufacturing* (2011). doi:[10.1007/s00170-010-2748-6](https://doi.org/10.1007/s00170-010-2748-6).
- [10] K. Mostafa, A. Qureshi, C. Montemagno, [Tolerance Control Using Subvoxel Gray-Scale DLP 3D Printing](#) (2017). doi:[10.1115/IMECE2017-72232](https://doi.org/10.1115/IMECE2017-72232).
450 URL <https://doi.org/10.1115/IMECE2017-72232>
- [11] C. Zhou, Y. Chen, R. A. Waltz, Optimized Mask Image Projection for Solid Freeform Fabrication, *Journal of Manufacturing Science and Engineering* (2009). doi:[10.1115/1.4000416](https://doi.org/10.1115/1.4000416).
- [12] C. Zhou, Y. Chen, Additive manufacturing based on optimized mask video projection for improved accuracy and resolution, *Journal of Manufacturing Processes* (2009). doi:[10.1016/J.JMAPRO.2011.10.002](https://doi.org/10.1016/J.JMAPRO.2011.10.002).
455

- [13] Z. D. Pritchard, M. P. Beer, R. J. Whelan, T. F. Scott, M. A. Burns, [Modeling and Correcting Cure-Through in Continuous Stereolithographic 3D Printing](#), *Adv. Mater. Technol.* 4 (12) (2019) 1900700. doi:10.1002/admt.201900700.
URL <https://onlinelibrary.wiley.com/doi/abs/10.1002/admt.201900700>
- 460 [14] J. Bonada, A. Muguruza, X. Fernández-Francos, X. Ramis, Optimisation procedure for additive manufacturing processes based on mask image projection to improve Z accuracy and resolution, *Journal of Manufacturing Processes* (2018). doi:10.1016/j.jmapro.2018.01.004.
- [15] Y. Wang, D. Xue, D. Mei, [Projection-Based Continuous 3D Printing Process With the Grayscale Display Method](#), *J. Manuf. Sci. Eng.* 142 (2) (feb 2020). doi:10.1115/1.4045616.
465 URL <https://asmedigitalcollection.asme.org/manufacturingscience/article/doi/10.1115/1.4045616/1071462/ProjectionBased-Continuous-3D-Printing-Process>
- [16] K. M. Lichade, E. B. Joyee, Y. Pan, Gradient light video projection-based stereolithography for continuous production of solid objects, *Journal of Manufacturing Processes* (2021). doi:10.1016/j.jmapro.2021.02.048.
- 470 [17] S. You, J. Guan, J. Alido, H. H. Hwang, R. Yu, L. Kwe, H. Su, S. Chen, Mitigating Scattering Effects in Light-Based Three-Dimensional Printing Using Machine Learning, *Journal of Manufacturing Science and Engineering* (2020). doi:10.1115/1.4046986.
- [18] K. S. Bhole, B. Kale, Techniques to minimise stair-stepping effect in micro-stereolithography process: A review, *Advances in Materials and Processing Technologies* (2021). doi:10.1080/2374068X.2021.1970997.
475
- [19] K. G. Mostafa, M. Arshad, A. Ullah, D. S. Nobes, A. J. Qureshi, Concurrent modelling and experimental investigation of material properties and geometries produced by projection microstereolithography, *Polymers* (2020). doi:10.3390/polym12030506.
- [20] M. M. Emami, D. W. Rosen, An Improved Vat Photopolymerization Cure Model Demonstrates Photobleaching Effects, 2018 International Solid Freeform Fabrication Symposium (2018). doi:10.26153/tsw/17195.
480
- [21] M. M. Emami, M. Jamshidian, D. W. Rosen, Multiphysics Modeling and Experiments of Grayscale Photopolymerization With Application to Microlens Fabrication, *Journal of Manufacturing Science and Engineering* (2021). doi:10.1115/1.4050549.
- 485 [22] M. M. Emami, D. W. Rosen, Modeling of light field effect in deep vat polymerization for grayscale lithography application, *Additive Manufacturing* (2020). doi:10.1016/j.addma.2020.101595.

- [23] A. Limaye, D. Rosen, Process planning method for mask projection micro-stereolithography, *Rapid Prototyping Journal* (2007). doi:[10.1108/13552540710736759](https://doi.org/10.1108/13552540710736759).
- [24] Y. Li, Q. Mao, J. Yin, Y. Wang, J. Fu, Y. Huang, Theoretical prediction and experimental validation of the digital light processing (DLP) working curve for photocurable materials, *Additive Manufacturing* (2020). doi:[10.1016/j.addma.2020.101716](https://doi.org/10.1016/j.addma.2020.101716).
- [25] S. Westbeek, J. Remmers, J. van Dommelen, H. Maalderink, M. Geers, [Prediction of the deformed geometry of vat photo-polymerized components using a multi-physical modeling framework](#), *Additive Manufacturing* 40 (2021) 101922. doi:<https://doi.org/10.1016/j.addma.2021.101922>.
URL <https://www.sciencedirect.com/science/article/pii/S2214860421000877>
- [26] Z. Ali, E. Tureyen, Y. Karpat, M. Cakmakci, Fabrication of Polymer Micro Needles for Transdermal Drug Delivery System Using DLP Based Projection Stereo-lithography, *Procedia CIRP* (2016). doi:[10.1016/j.procir.2016.02.194](https://doi.org/10.1016/j.procir.2016.02.194).
- [27] Y. Li, Q. Mao, X. Li, J. Yin, Y. Wang, J. Fu, Y. Huang, High-fidelity and high-efficiency additive manufacturing using tunable pre-curing digital light processing, *Additive Manufacturing* (2019). doi:[10.1016/j.addma.2019.100889](https://doi.org/10.1016/j.addma.2019.100889).
- [28] R. Wicker, F. Medina, C. Elkins, Multiple Material Micro-Fabrication: Extending Stereolithography to Tissue Engineering and Other Novel Applications, 2004 International Solid Freeform Fabrication Symposium (2004). doi:[10.26153/tsw/7038](https://doi.org/10.26153/tsw/7038).
- [29] E. Tureyen, Y. Karpat, M. Cakmakci, [Development of an iterative learning controller for polymer based micro-stereolithography prototyping systems](#), in: 2016 Am. Control Conf., Vol. 2016-July, IEEE, 2016, pp. 852–857. doi:[10.1109/ACC.2016.7525020](https://doi.org/10.1109/ACC.2016.7525020).
URL <http://ieeexplore.ieee.org/document/7525020/>
- [30] Texas Instruments, DLP4710 0.47 1080p DMD datasheet (Rev. A) (11 2021).